ELSEVIER

Applied Ocean Research 23 (2001) 319–336

Applied Ocean Research

www.elsevier.com/locate/apor

A coupled-mode model for the refraction–diffraction of linear waves over steep three-dimensional bathymetry

K.A. Belibassakis*, G.A. Athanassoulis, Th.P. Gerostathis

Department of Naval Architecture and Marine Engineering, National Technical University of Athens, P.O. Box 64033, Zografos, 15710 Athens, Greece

Received 30 July 2001; accepted 11 February 2002

Abstract

A consistent coupled-mode model recently developed by Athanassoulis and Belibassakis [1], is generalized in 2 + 1 dimensions and applied to the diffraction of small-amplitude water waves from localized three-dimensional scatterers lying over a parallel-contour bathymetry. The wave field is decomposed into an incident field, carrying out the effects of the background bathymetry, and a diffraction field, with forcing restricted on the surface of the localized scatterer(s). The vertical distribution of the wave potential is represented by a uniformly convergent local-mode series containing, except of the ususal propagating and evanescent modes, an additional mode, accounting for the sloping bottom boundary condition. By applying a variational principle, the problem is reduced to a coupled-mode system of differential equations in the horizontal space. To treat the unbounded domain, the Berenger perfectly matched layer model is optimized and used as an absorbing boundary condition. Computed results are compared with other simpler models and verified against experimental data. The inclusion of the sloping-bottom mode in the representation substantially accelerates its convergence, and thus, a few modes are enough to obtain accurately the wave potential and velocity up to and including the boundaries, even in steep bathymetry regions. The present method provides high-quality information concerning the pressure and the tangential velocity at the bottom, useful for the study of oscillating bottom boundary layer, sea-bed movement and sediment transport studies. © 2002 Published by Elsevier Science Ltd.

Keywords: Coupled-mode model; Refraction–diffraction; Sloping-bottom

1. Introduction

The interaction of free-surface gravity waves with an uneven bottom topography, e.g. a shoaling, containing localized three-dimensional (3D) irregularities, in water of intermediate depth, is a mathematically difficult problem for which a broad class of approximation techniques has been developed. This problem is complicated by the fact that the physical properties of the medium (the wavenumber and the propagation speed) are different at infinity in different directions. In this case the far-field wave pattern is not known a priori, and a standard radiation condition cannot be applied.

In the case when the bed is mildly sloping in the region under consideration, approximate one-equation models, such as the classical mild-slope equation [2,3], or the modified mild-slope equation [4–6], can be used for the description of wave propagation and diffraction. Such models have been widely used to predict the wave field in coastal regions, since they are able to treat bottom topographies with satisfactory accuracy for bottom slopes up to 1:3, or even higher [7,8]. Applications of these models to 3D scattering problems have been presented by various authors using various numerical techniques, such as the finite element method [9,10], and the angular spectrum model [11,12]. The works by Panchang et al. [13], Li [14], Zhao and Anastasiou [15] and Oliveira and Anastasiou [16], are all based on the discretization of the elliptic mild-slope equation by finite differences, leading to large, sparse systems of equations. The main innovation of the latter works is that the numerical solutions are obtained by applying sophisticated iterative methods, such as the generalized conjugate gradient method, the stabilized bi-conjugate gradient method and the generalized minimum residual method. Li and Anastasiou [17] proposed an alternative model based on an exponential transformation of the unknown wave field to a slowly varying phase function, resulting in a non-linear equation. A notable feature of all the above works is that they are formulated with respect to the total wave potential.

The basic restriction inherent to any one-equation model is that the vertical structure of the wave field is given by a specific, preselected function. This restriction makes them inappropriate to describe the wave field when the bottom topography contains steep elements and/or

* Corresponding author. Fax: +30-10-7721032.
E-mail address: kbel@fluid.mech.ntua.gr (K.A. Belibassakis).

0141-1187/02/$ - see front matter © 2002 Published by Elsevier Science Ltd.
PII: S0141-1187(02)00004-4

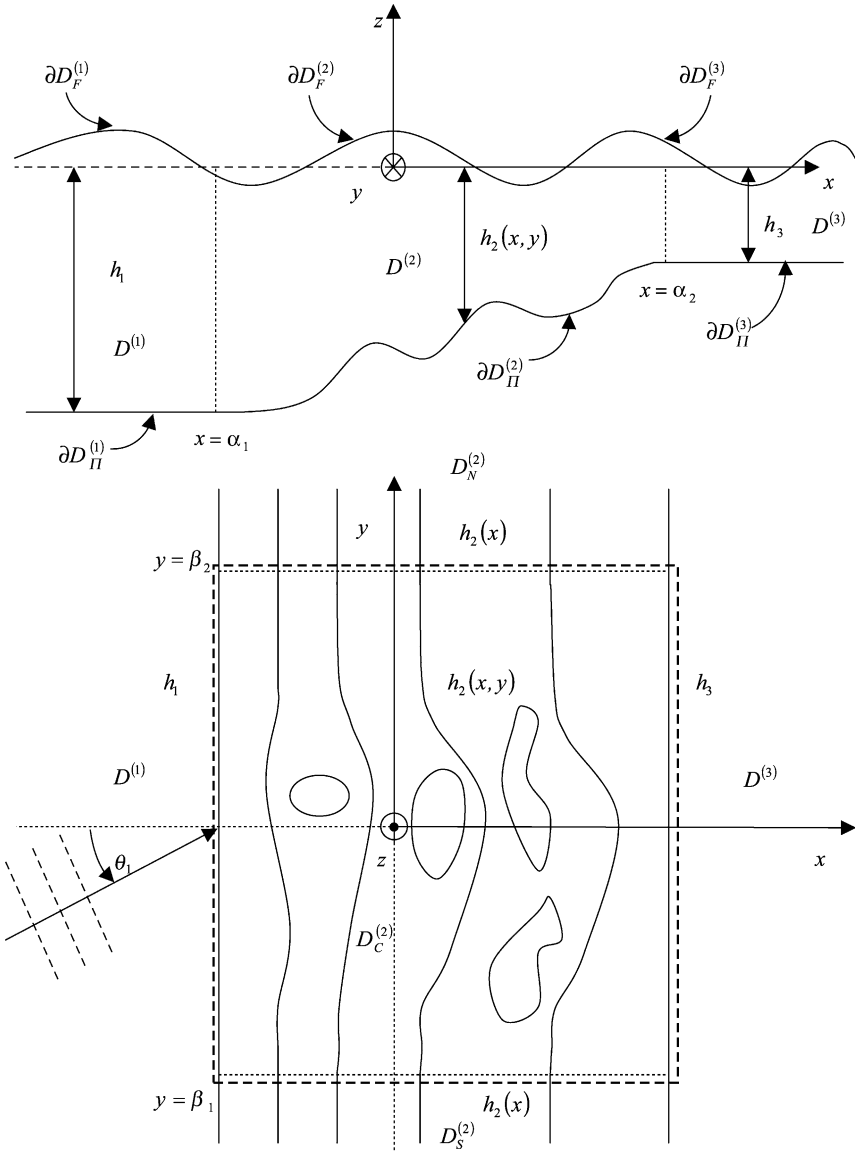

Fig. 1. Domain decomposition and basic notation.

localized scatterers in waters of intermediate depth. The improvement of the mild-slope models to match the requirements of this situation calls for a more general representation of the vertical structure of the wave field. Massel [5] and Porter and Staziker [18] presented this kind of models, called extended mild-slope equations, in which the vertical profile of the wave potential at any horizontal position is represented by a local-mode series involving the propagating and all evanescent modes, leading to an infinite coupled-mode system of equations. See also the survey by Porter and Chamberlain [19]. However, this expansion is inconsistent with the Neumann condition on a sloping bottom, since each of the vertical modes involved in the local-mode series violates it and, thus, the solution, being a linear superposition of modes, behaves the same. This fact has two important consequences. First, the velocity field in the vicinity of the bottom is poorly represented and, secondly, wave energy is not generally conserved. This problem has been remedied by the consistent coupled-mode theory recently developed by Athanassoulis and Belibassakis [1]. In the latter work the standard local-mode representation is enhanced by including an additional term, called the sloping-bottom mode, leading to an enhanced coupled-mode system of equations. This model is free of any simplifications concerning the vertical structure of the wave field and of any assumptions concerning the bottom slope and curvature, and it is consistent since it enables the exact satisfaction of the bottom boundary condition and the conservation of energy. Moreover, the consistent coupled-mode theory provides an improved decay of the model-amplitude functions of order $O(n^{-4})$, where n is the mode number. Thus, in most practical applications, a few (e.g. 3–5) modes is sufficient to accurately calculate the complete 3D velocity field up to (and including) the boundaries. The importance of the

exact satisfaction of the sloping bottom boundary condition by linear refraction–diffraction models applied to steep bathymetry has been recently demonstrated also by Chandrasekera and Cheung [20]. In this work an approximate two-equation model is presented, where the second equation takes care for the exact satisfaction of the sea-bed boundary condition, showing significant enhancement of numerical predictions in comparison to one-equation models.

In the present work, the consistent coupled-mode formulation is applied to the complete linear problem of propagation–refraction–diffraction of water waves in an intermediate-depth coastal environment. The examined environment consists of a transition region lying between two areas of constant but different depth, and containing the localized 3D inhomogeneities; see Fig. 1. A specific feature of the present work is the decomposition of the problem to an incident field carrying out the effects of the parallel-contour bathymetry, and a diffraction field carrying out the effects of the localized scatterer(s). It should be noted that, in this case, the incident field is not given (known) a priori, but it is calculated separately, as a first step in the solution procedure. This is accomplished by applying the consistent coupled-mode theory [1] to the case of an obliquely incident monochromatic wave coming from the offshore constant-depth region in the absence of the localized scatterer(s). The diffraction problem is then treated by applying a similar approach. In this way, the forcing associated with the diffraction problem is restricted only on the support of the localized scatterer(s). Working with the diffraction potential in 3D applications is very beneficial from the numerical point of view (described later).

A prominent difficulty that remains to be tackled is associated with the unboundness of the domain and the lack of a specific radiation condition. As concerns the far-field structure of the diffraction potential, first results have been obtained by studying the problem of a pulsating source over a two-dimensional, uneven bottom topography, with different depths at infinity, in Athanassoulis and Belibassakis [21] and Belibassakis [22]. In these works it is shown that, in the case of a monotonic bed profile, the far-field generated by a source located in the variable bathymetry region contains a shadow zone with an expanding width in the transverse direction, i.e. along with the straight-line bottom contours of the background bathymetry. Moreover, in each of the two sectors not including the bottom shoaling area the asymptotic behaviour of the wave field approaches the form of an outgoing cylindrical wave, with amplitude of order $O(R^{-1/2})$, where R is the horizontal distance from the source, and wavelength corresponding to the sector-depth at infinity. On the contrary, localized disturbances over non-monotonic bed profiles can generate duct propagation along the bottom irregularity, since trapping modes exist in this case; see Mei [3].

To tackle the problem of the unbounded domain, the following numerical techniques are used in practice: the artificial or non-reflecting boundary conditions (ABCs or NRBCs), the absorbing layers and the infinite elements. All the above are introduced in conjunction with an artificial exterior boundary in order to eliminate the infinite domain, absorbing at the same time the wave energy that reaches the artificial boundary; see the surveys by Givoli [23], Dalrymple and Martin [24] and Tsynkov [25]. The absorbing layer technique occupies an intermediate position between the high-quality, global NRBCs, which are the hardest to construct and the most expensive to implement, and the local ones, which are the cheapest and the less accurate ones (Tsynkov [25]. In the present work the Perfectly Matched Layer (PML) model, introduced by Berenger [26] for the absorption of electromagnetic waves, and formulated for general elliptic equations by Turkel and Yefet [27] and by Collino and Monk [28], is applied as the closure condition to the diffraction problem. Restricting ourselves to the class of monotonic background bed profiles, for which evidence exists that the solution of the diffraction problem is composed only of decaying outgoing waves, the PML technique is a good compromise to the requirements of error minimization and low computational cost.

The present work is structured as follows: In Section 2 the complete, linearized, boundary-value problem is considered in the frequency domain. Since the water layer extends to infinity in the horizontal directions, the assumption is made that far ahead and behind the scatterer(s) the depth is eventually constant (although may be different in different directions). In Section 3 the consistent coupled-mode system for obtaining the solution to the incident problem is presented (the *i*-system). In Section 4 a variational formulation of the diffraction problem is given and applied, in conjunction with the enhanced local-mode representation of the diffraction field, to obtain the consistent coupled-mode system of horizontal equations for the diffraction problem (*d*-system). To restrict the support of the *d*-system in a bounded domain containing the localized scatterer(s), in Section 5, the PML model is adopted and optimized to serve as the closure condition of the system. In Section 6 the approximate solution of the problem is obtained by truncating the enhanced local-mode series into a finite number of terms, retaining the propagating, the sloping-bottom and a sufficient number of evanescent modes to achieve numerical convergence. The truncated coupled-mode systems are numerically solved by using a second-order finite difference scheme. Numerical results are presented for the case of the Berkhoff elliptic shoal [9], and compared with the experimental data and numerical results obtained by means of the modified mild-slope equation. To illustrate the performance of the present method for the case of non-mildly sloped bathymetries, a second bottom geometry, corresponding to a steep platform reef with bottom corrugations, is examined, and the obtained results have been compared with the corresponding ones obtained by the modified mild-slope equation. Noticeable differences have been detected, which are attributed to fine-scale three-dimensional wave-bottom

interactions that cannot be well resolved by the modified mild-slope equation.

2. Formulation of the problem

The studied marine environment consists of a water layer D bounded above by the free surface ∂D_{F} and below by a rigid bottom ∂D_{Π}. It is assumed that the bottom surface exhibits an arbitrary variation in a bounded subdomain, which includes the support of the localized scatterer(s). Outside this area, the bathymetry is characterized by parallel, straight bottom contours lying between two regions of constant but different depth, $h = h_1$ (region of incidence) and $h = h_3$ (region of transmission); see Fig. 1. The liquid is assumed homogeneous, inviscid and incompressible. The wave field is excited by a monochromatic plane wave of angular frequency ω, propagating with an oblique direction θ_1 with respect to the bottom contours (the oblique-incident wave). In this case, the most important non-dimensional characteristic numbers are: the shallowness ratio h/λ, where h is the local depth and λ is the local wavelength, the bottom slope, and the shoaling ratio h/h_1. In the present work all these non-dimensional numbers are considered to be of the same order of magnitude.

A Cartesian coordinate system is introduced, with its origin at some point on the mean water level (in the variable bathymetry region), the z-axis pointing upwards. The liquid domain D is decomposed in three areas $D^{(m)}$, $m = 1, 2, 3$ (Fig. 1), defined as follows: $D^{(1)}$ is the subdomain characterized by $x < \alpha_1$ where the depth is constant and equal to h_1, $D^{(3)}$ is the subdomain characterized by $x > \alpha_2$ ($\alpha_1 < \alpha_2$) where the depth is constant and equal to h_3, and $D^{(2)}$ is the variable bathymetry subdomain lying between $D^{(1)}$ and $D^{(3)}$. Furthermore, $D^{(2)}$ can be decomposed in three areas $D_{\mathrm{S}}^{(2)}$, $D_{\mathrm{C}}^{(2)}$, $D_{\mathrm{N}}^{(2)}$ as follows: the central part $D_{\mathrm{C}}^{(2)}$ containing the localized scatterer(s), characterized by $\alpha_1 < x < \alpha_2$ and $\beta_1 < y < \beta_2$, where the bathymetry exhibits a two dimensional variation $h_2(x, y)$, the part $D_{\mathrm{S}}^{(2)}$ characterized by $\alpha_1 < x < \alpha_2$ and $y < \beta_1$, and the part $D_{\mathrm{N}}^{(2)}$ characterized by $\alpha_1 < x < \alpha_2$ and $y < \beta_2$, where the bathymetry $h_2(x)$ presents variability only along the x-axis. On the basis of the above definitions, the depth function is decomposed as follows

$$h(x, y) = h_i(x) + h_{\mathrm{d}}(x, y), \tag{2.1}$$

where

$$h_i(x) = \begin{cases} h_1, & x \le \alpha_1 \\ h_2(x), & \alpha_1 < x < \alpha_2, \ \text{and support}(h_{\mathrm{d}}) \subset D_{\mathrm{C}}^{(2)} \\ h_3, & x \ge \alpha_3 \end{cases} \tag{2.2}$$

Clearly, $h_{\mathrm{d}}(x, y)$ is the disturbance of the parallel-contour surface $z = -h_i(x)$ produced by the localized scatterer(s) in $D_{\mathrm{C}}^{(2)}$. We assume that $h(x, y)$ is continuously differentiable. The above decomposition is also applied to the boundaries ∂D_{F} and ∂D_{Π} (Fig. 1). Without loss of generality, we assume that $h_1 > h_3$, i.e. $D^{(1)}$ is the deep water region and $D^{(3)}$ is the shallow-water region. Assuming also that the free-surface elevation and the velocity field are small, the fluid motion can be described by a harmonic velocity potential of the form

$$\Phi(x, y, z; t) = \mathrm{Re}\left\{ -\frac{\mathrm{i}gH}{2\omega}\, \phi(x, y, z; \mu) \exp(-\mathrm{i}\omega t) \right\}, \tag{2.3}$$

where ω is the angular frequency, g is the acceleration due to gravity, $\mu = \omega^2/g$ is the frequency parameter, H is the oblique-incident wave height and $\mathrm{i} = \sqrt{-1}$. The function $\phi = \phi(x, y, z; \mu)$ is the normalized potential in the frequency domain, usually written as $\phi(x, y, z)$. Under the previous assumptions the classical (differential) formulation of the boundary value problem is stated as follows:

$$\left(\frac{\partial^2}{\partial z^2} + \nabla^2 \right) \phi(x, y, z) = 0, \qquad (x, y, z) \in D, \tag{2.4a}$$

$$\frac{\partial \phi}{\partial z} - \mu \phi = 0, \qquad \mu = \frac{\omega^2}{g} > 0, \ (x, y, z) \in \partial D_{\mathrm{F}}, \tag{2.4b}$$

$$\left(\frac{\partial}{\partial z} + \nabla h \nabla \right) \phi = 0, \qquad (x, y, z) \in \partial D_{\Pi}, \tag{2.4c}$$

$\phi(x, y, z)$ and its derivatives remain bounded as

$$R = \sqrt{x^2 + y^2} \to \infty, \tag{2.4d}$$

where $\nabla = (\partial/\partial x, \partial/\partial y)$ is the horizontal gradient operator. The above problem is forced by the oblique-incident wave, characterized by the potential

$$\phi_{\mathrm{oi}}(x, y, z) = \exp(\mathrm{i}(\kappa_x x + \kappa_y y)) \frac{\cosh\left(k_0^{(1)}(z + h_1)\right)}{\cosh\left(k_0^{(1)} h_1\right)}, \tag{2.5a}$$

$(x, y, z) \in D^{(1)}$.

The wavenumber vector of the oblique-incident wave is

$$\kappa_x \vec{i} + \kappa_y \vec{j} = k_0^{(1)} \cos\theta_1 \vec{i} + k_0^{(1)} \sin\theta_1 \vec{j}, \tag{2.5b}$$

where $k_0^{(1)}$ is the positive root of the dispersion relation $\mu h_1 = k_0^{(1)} h_1 \tanh(k_0^{(1)} h_1)$ in $D^{(1)}$, and $\vec{i}$, $\vec{j}$ are the unit normal vectors along the axes x and y, respectively.

2.1. Formulation of the incident and the diffraction problems

Exploiting the linearity of the problem (2.4a)–(2.4d) and the depth definition (2.1), the total wave potential $\phi(x, y, z)$ can be decomposed in two parts, the potential $\phi_i(x, y, z)$ representing the propagation over the parallel-contour surface $h_i(x)$, which will be called the incident wave field, and the potential $\phi_{\mathrm{d}}(x, y, z)$ representing the diffraction field

by the 3D localized bathymetric features $h_d(x, y)$,

$$\phi(x, y, z) = \phi_i(x, y, z) + \phi_d(x, y, z). \tag{2.6}$$

On the basis of physical grounds we assume that, since the oblique-incident wave (Eqs. (2.5a) and (2.5b)) is periodic along the y-direction, the incident potential $\phi_i(x, y, z)$ is also y-periodic with the same wavelength $\lambda = 2\pi/\kappa_y$, where $\kappa_y = k_0^{(1)} \sin\theta_1$; see Kirby and Dalrymple [29], Massel [5]. Thus, by introducing the factorization

$$\phi_i(x, y, z) = e^{i\kappa_y y}\varphi_i(x, z), \tag{2.7}$$

we obtain the following two-dimensional problem for $\varphi_i(x, z)$:

$$\frac{\partial^2\varphi_i(x,z)}{\partial x^2} + \frac{\partial^2\varphi_i(x,z)}{\partial z^2} - \kappa_y^2\varphi_i(x,z) = 0, \quad -\infty < x < \infty, \ -h_i(x) < z < 0, \tag{2.8a}$$

$$\frac{\partial\varphi_i(x,z)}{\partial z} - \mu\varphi_i(x,z) = 0, \qquad -\infty < x < \infty, \ z = 0, \tag{2.8b}$$

$$\left(\frac{\partial}{\partial z} + \frac{dh_i}{dx}\frac{\partial}{\partial x}\right)\varphi_i(x,z) = 0, \quad -\infty < x < \infty, \ z = -h_i(x), \tag{2.8c}$$

supplemented by the radiation conditions

$$\varphi_i(x,z) \to \left[e^{ik_0^{(1)}\cos\theta_1 x} + A_R\, e^{-ik_0^{(1)}\cos\theta_1 x}\right] \times \frac{\cosh\left(k_0^{(1)}(z+h_1)\right)}{\cosh\left(k_0^{(1)}h_1\right)}, \ x \to -\infty, \tag{2.8d}$$

$$\varphi_i(x,z) \to A_T\, e^{ik_0^{(3)}\cos\theta_3 x}\frac{\cosh\left(k_0^{(3)}(z+h_3)\right)}{\cosh\left(k_0^{(3)}h_3\right)}, \qquad x \to \infty. \tag{2.8e}$$

In the above equations, A_R and A_T are the reflection and transmission coefficients, respectively. The direction of the transmitted wave in $D^{(3)}$ is given by

$$\theta_3 = \sin^{-1}\left(k_0^{(1)}\sin\theta_1/k_0^{(3)}\right); \tag{2.8f}$$

see also Massel [5]. The wavenumbers $k_0^{(m)}$ $m = 1, 3$, appearing in Eqs. (2.8a)–(2.8f) are obtained by the corresponding dispersion relations

$$\mu h_m = k_0^{(m)}h_1 \tanh\left(k_0^{(m)}h_m\right), \qquad m = 1, 3, \tag{2.9}$$

formulated at the depths h_m, $m = 1, 3$, respectively.

By substituting the decomposition (2.6) in Eqs. (2.4a)–(2.4d) and using Eqs. (2.7) and (2.8a)–(2.8f), we obtain the following problem for the diffraction potential $\phi_d(x, y, z)$:

$$\left(\frac{\partial^2}{\partial z^2} + \nabla^2\right)\phi_d(x, y, z) = 0, \qquad (x, y, z) \in D \tag{2.10a}$$

$$\frac{\partial\phi_d}{\partial z} - \mu\phi_d = 0, \qquad \mu = \frac{\omega^2}{g} > 0, \ (x, y, z) \in \partial D_F, \tag{2.10b}$$

$$\left(\frac{\partial}{\partial z} + \nabla h\nabla\right)\phi_d = g(x, y) = -\left(\frac{\partial}{\partial z} + \nabla h\nabla\right)\phi_i, \quad (x, y, z) \in \partial D_\Pi, \tag{2.10c}$$

supplemented by the radiation condition requiring that ϕ_d behaves like outgoing waves as

$$R = \sqrt{x^2 + y^2} \to \infty. \tag{2.10d}$$

It is obvious that the support of the forcing $g(x, y)$ of diffraction problems (2.10a)–(2.10d) is exactly the same as the support of the localized scatterer(s).

It must be noted here that, although a solution of the present problem based on the formulation with respect to the total wave potential, Eqs. (2.4a)–(2.4d), is possible, working with the diffraction potential is much more efficient from the numerical point of view. To better understand this assertion, consider the simple case of scattering of a plane incident wave by a submerged circular sill in constant depth. In this case an analytical solution is available in cylindrical coordinates in the form of infinite series involving Bessel and Hankel functions (Longuet-Higgins [30], see also Mei [3], Section 4.9.2). From this solution it is evident that the number of azimuthal modes required for the numerical convergence of the total wave field is of the order $O(kR)$, where k is the propagating wavenumber, while the diffraction potential requires only $O(k\rho_{sc})$ terms, where ρ_{sc} is the radius of the scatterer. Thus, the numerical efficiency of the series representing the diffraction field is uniform in space, while the numerical efficiency of the total field series degrades as the distance from the scatterer(s) increases.

2.2. The far-field structure of the diffraction potential

The radiation condition (2.10d) will be now put in a more explicit form. To this aim, we need more information concerning the far-field structure of the diffraction potential ϕ_d. This question is answered with the aid of the appropriate Green's function $G(\vec{r}; \vec{r}_0)$, representing the pulsating-source potential over the background (parallel-contour) bathymetry, which has been studied by Athanassoulis and Belibassakis [21] and Belibassakis [22]. In the latter works, the following far-field asymptotic results have been

established:

$$G(\vec{r},\vec{r}_0) = F_m(\theta)\frac{\exp\left(\mathrm{i}\,k_0^{(m)}R_h\right)}{\sqrt{R_h}}\frac{\cosh\left(k_0^{(m)}(z+h_m)\right)}{\cosh\left(k_0^{(m)}h_m\right)} + \mathrm{O}\left(R_h^{-3/2}\right), \tag{2.11a}$$

$$\vec{r}\in D^{(m)},\ m=1,3,$$

$$G(\vec{r},\vec{r}_0) = \mathrm{O}\left(R_h^{-3/2}\right), \qquad \vec{r}\in D^{(2)}, \tag{2.11b}$$

under the assumptions that

(i) the source point $\vec{r}_0=(x_0,y_0,z_0)$ lies in the variable bathymetry subdomain $D^{(2)}$;
(ii) the field point $\vec{r}=(x,y,z)$ is far from $\vec{r}_0$, in the sense that $R_h=\sqrt{(x-x_0)^2+(y-y_0)^2}\to\infty$, i.e. R_h is large in comparison with the characteristic wave lengths;
(iii) the depth function $h_i(x)$ is monotonic (to ensure that trapping modes are not excited).

In Eqs. (2.11a) and (2.11b), $\theta=\tan^{-1}((y-y_0)/(x-x_0))$ and $F_m(\theta)$ is the far-field pattern of the source potential in $D^{(m)}$, $m=1,3$, which is independent from R_h. On the basis of the above asymptotics, the following results are obtained concerning the far-field behaviour of the diffraction potential ϕ_d:

(i) In each sector lying entirely in $D^{(m)}$ $m=1,3$, the asymptotic behaviour of the diffraction field approaches the form of an outgoing cylindrical wave, propagating with wavelength corresponding to the sector-depth at infinity. In these sectors the diffraction field exhibits a decay $\phi_\mathrm{d}=\mathrm{O}(R^{-1/2})$, $R\to\infty$, $\vec{r}\in D^{(m)}$, $m=1,3$, and obeys the standard (Sommerfeld) radiation condition

$$\frac{\partial\phi_\mathrm{d}}{\partial R}-\mathrm{i}k_0^{(m)}\phi_\mathrm{d}=\mathrm{O}(R^{-3/2}),\quad R\to\infty,\ \vec{r}\in D^{(m)},\ m=1,3. \tag{2.12a}$$

(ii) Along the bottom irregularity in $D^{(2)}$, i.e. as θ approaches $\theta=\pi/2$, the diffraction field exhibits a faster decay

$$\frac{\partial\phi_\mathrm{d}}{\partial y}=\mathrm{O}(R^{-3/2}), \qquad R\to\infty,\ \vec{r}\in D^{(2)}. \tag{2.12b}$$

Eqs. (2.12) and (2.12b), taken together, express analytically the appropriate radiation condition of the diffraction problem (2.10a)–(2.10d). Note that, the far-field behaviour of ϕ_d is anisotropic with respect to θ.

3. The coupled-mode system of equations for the incident-field problem

The problem on $\varphi_i(x,z)$, Eqs. (2.8a)–(2.8f), will be treated by means of the consistent coupled mode theory [1]. This theory is based on the following enhanced local-mode representation of the incident field (in the absence of the localized scatterers):

$$\varphi_i(x,z)=\varphi_{-1}(x)Z_{-1}(z;x)+\varphi_0(x)Z_0(z;x)+\sum_{n=1}^{\infty}\varphi_n(x)Z_n(z;x). \tag{3.1}$$

In Eq. (3.1) the term $\varphi_0(x)Z_0(z;x)$ is the propagating mode of the incident field and will be called the *i*-propagating mode. The remaining terms $\varphi_n(x)Z_n(z;x)$, $n=1,2,\ldots$ are the evanescent modes, and the additional term $\varphi_{-1}(x)Z_{-1}(z;x)$ is a correction term called the sloping-bottom mode, which accounts for the bottom boundary condition on a sloping bottom. The function $Z_n(z;x)$ represents the vertical structure of the nth mode. The function $\varphi_n(x)$ describes the horizontal pattern of the nth mode and is called the complex amplitude of the nth mode. The functions $Z_n(z;x)$, $n=0,1,2,\ldots$ appearing in Eq. (3.1) are obtained as the eigenfunctions of local vertical Sturm–Liouville problems, and are given by

$$Z_0(z;x)=\frac{\cosh[k_0(x)(z+h_i(x))]}{\cosh(k_0(x)h_i(x))},\qquad Z_n(z;x)=\frac{\cos[k_n(x)(z+h_i(x))]}{\cos(k_n(x)h_i(x))},\quad n=1,2,\ldots, \tag{3.2a}$$

where the eigenvalues $\{\mathrm{i}k_0(x),k_n(x)\}$ are obtained as the roots of the dispersion relation

$$\mu h_i(x)=-k(x)h_i(x)\cdot\tan[k(x)h_i(x)],\qquad \alpha_1\le x\le\alpha_2. \tag{3.2b}$$

The necessity for enhancing the local-mode series by including the sloping-bottom mode $\varphi_{-1}(x)Z_{-1}(z;x)$, in the case of a steep bathymetry, has been described in detail in Ref. [1]. The vertical structure $Z_{-1}(z;x)$ of this additional mode has to be smooth z-function in $[-h_i(x),0]$, satisfying the conditions

$$\frac{\partial Z_{-1}(z=0,x)}{\partial z}-\mu Z_{-1}(z=0,x)=0,\qquad \frac{\partial Z_{-1}(z=-h(x),x)}{\partial z}=1. \tag{3.3a}$$

We remark that the first of the above conditions implies that $\varphi_{-1}(x)Z_{-1}(z;x)$ satisfies the free-surface condition, and second one, in conjunction with Eq. (3.2a) and the representation (3.1), implies that

$$\varphi_{-1}(x)=\partial\varphi_i(x,z=-h_i(x))/\partial z. \tag{3.3b}$$

Thus, the sloping-bottom mode vanishes in constant-depth

subregions, where $\partial\varphi_i(x, z=-h_i(x))/\partial z = 0$. We also note here that $Z_{-1}(z;x)$ is not uniquely defined; however, this freedom does not affect the final results. For an extensive discussion about this issue the reader is referred to Ref. [1, Section 4]. A specific convenient form of $Z_{-1}(z;x)$ is given by

$$Z_{-1}(z;x) = h_i(x)\left[\left(\frac{z}{h_i(x)}\right)^3 + \left(\frac{z}{h_i(x)}\right)^2\right], \tag{3.3c}$$

and all numerical results presented in this work are based on this choice for $Z_{-1}(z;x)$. By following exactly the same procedure as in Ref. [1], the coupled-mode system for the incident wave field (the *i*-system) is obtained

$$\sum_{n=-1}^{\infty} a_{mn}(x)\varphi_n''(x) + b_{mn}(x)\varphi_n'(x) + \left(c_{mn}(x) - a_{mn}\kappa_y^2\right)\varphi_n(x) = 0,$$
$$\alpha_1 < x < \alpha_2, \quad m = -1, 0, 1, \ldots, \tag{3.4}$$

where a prime denotes differentiation with respect to x. The coefficients a_{mn}, b_{mn}, c_{mn} of the system (3.4) can be found in Table 1 of Ref. [1]. The system (3.4) is supplemented by the following boundary conditions [5]

$$\varphi_{-1}(\alpha_1) = \varphi'_{-1}(\alpha_1) = 0, \qquad \varphi_{-1}(\alpha_2) = \varphi'_{-1}(\alpha_2) = 0, \tag{3.5a}$$

$$\varphi_0'(\alpha_1) + \mathrm{i}\lambda_0^{(1)}\varphi_0(\alpha_1) = 2\mathrm{i}\lambda_0^{(1)}\exp\left(\mathrm{i}\lambda_0^{(1)}\alpha_1\right),$$
$$\varphi_n'(\alpha_1) - \lambda_n^{(1)}\varphi_n(\alpha_1) = 0, \quad n = 1, 2, \ldots, \tag{3.5b}$$

$$\varphi_0'(\alpha_2) - \mathrm{i}\lambda_0^{(3)}\varphi_0(\alpha_2) = 0,$$
$$\varphi_n'(\alpha_2) + \lambda_n^{(3)}\varphi_n(\alpha_2) = 0, \quad n = 1, 2, 3, \ldots, \tag{3.5c}$$

where the coefficients $\lambda_n^{(1)}$, $\lambda_n^{(3)}$, $n = 0, 1, 2, \ldots$ are given by

$$\lambda_0^{(1)} = k_0^{(1)}\cos\theta_1,$$
$$\lambda_n^{(1)} = \sqrt{\left(k_n^{(1)}\right)^2 + \left(k_0^{(1)}\sin\theta_1\right)^2}, \quad n = 1, 2\ldots, \tag{3.6a}$$

$$\lambda_0^{(3)} = k_0^{(3)}\cos\theta_3,$$
$$\lambda_n^{(3)} = \sqrt{\left(k_n^{(3)}\right)^2 + \left(k_0^{(3)}\sin\theta_3\right)^2}, \quad n = 1, 2\ldots. \tag{3.6b}$$

In the above equations θ_3 is defined by Eq. (2.8f), $\{\mathrm{i}k_0^{(1)}, k_n^{(1)}\}$ are the eigenvalues $\{\mathrm{i}k_0(x), k_n(x)\}_{x=\alpha_1}$, which remain the same all over the region $D^{(1)}$, and $\{\mathrm{i}k_0^{(3)}, k_n^{(3)}\}$ are the eigenvalues $\{\mathrm{i}k_0(x), k_n(x)\}_{x=\alpha_3}$, which remain the same all over the region $D^{(3)}$. The reflection and transmission coefficients $(A_\mathrm{R}, A_\mathrm{T})$ appearing in Eqs. (2.8d) and (2.8e) are calculated from the solution of the *i*-system by

$$A_\mathrm{R} = \left(\varphi_0(\alpha_1) - \exp\left(\mathrm{i}\lambda_0^{(1)}\alpha_1\right)\right)\exp\left(\mathrm{i}\lambda_0^{(1)}\alpha_1\right),$$
$$A_\mathrm{T} = \varphi_0(\alpha_2)\exp\left(-\mathrm{i}\lambda_0^{(3)}\alpha_2\right), \tag{3.7}$$

and the forcing term $g(x, y)$ of the diffraction problem is calculated by using Eq. (2.10c) in conjunction with Eqs. (2.7) and (3.1).

An important feature of the solution of the incident problem by means of the enhanced representation (3.1), is that it exhibits and improved rate of decay of the modal amplitudes $|\varphi_n(x)|$ of the order $\mathrm{O}(n^{-4})$. Thus, a small number of modes suffices to obtain a convergent solution to $\varphi_i(x, z)$, even for bottom slopes of the order of 1:1, or higher; see the results presented in Section 6 of Ref. [1].

4. The coupled-mode system of equations for the diffraction problem

In this section the corresponding coupled-mode system of horizontal equations for the diffraction problem (the *d*-system) will be derived from a variational principle. This principle, first introduced by Bai [31] for the diffraction by localized scatterer(s) in constant depth (see also Bai and Yeung [32], Yeung [33]), is an approximate one, due to the fact that the radiation conditions are applied to a vertical boundary located at a large but finite distance from the scatterer(s). In this way, the exact problem, Eqs. (2.10a)–(2.10c), formulated in a truncated domain $\tilde{D}(R_\infty)$ consisting of a finite part of the strip $D^{(2)}$ (containing the localized scatterers) and two semi-circular finite cylinders of large radius R_∞ lying in $D^{(1)}$ and $D^{(3)}$, respectively. At a later stage (Section 5), these closure conditions will be further improved by using optimal absorbing layers.

4.1. The variational principle

To start with, consider the functional

$$\mathscr{F}(\phi_\mathrm{d}) = \frac{1}{2}\int_{\tilde{D}(R_\infty)} (\nabla\phi_\mathrm{d})^2\,\mathrm{d}V - \frac{1}{2}\mu\int_{\partial\tilde{D}_\mathrm{F}(R_\infty)} (\phi_\mathrm{d})^2\,\mathrm{d}S$$
$$- \frac{\mathrm{i}k_0^{(1)}}{2}\int_{\partial\tilde{D}_V^{(1)}(R_\infty)} (\phi_\mathrm{d})^2\,\mathrm{d}S - \frac{\mathrm{i}k_0^{(3)}}{2}\int_{\partial\tilde{D}_V^{(3)}(R_\infty)} (\phi_\mathrm{d})^2\,\mathrm{d}S$$
$$+ \int_{\partial\tilde{D}_\Pi(R_\infty)} g\phi_\mathrm{d}\,\mathrm{d}S, \tag{4.1}$$

where $k_0^{(1)}$, $m = 1, 3$, are obtained by the dispersion relation (2.9), and g is the forcing of the diffraction problem defined by Eq. (2.10c). In Eq. (4.1), $\partial\tilde{D}_\mathrm{F}(R_\infty)$ is the part of the free surface contained in $\tilde{D}(R_\infty)$, $\partial\tilde{D}_\Pi(R_\infty)$ is the part of the bottom surface contained in $\tilde{D}(R_\infty)$, and $\partial\tilde{D}_V^{(m)}(R_\infty)$, $m = 1, 3$, are the vertical parts of the boundary of the semi-circular cylinders lying in the subdomains $D^{(m)}$, $m = 1, 3$, respectively. By restricting the admissible function space

Table 1
Coefficients of the *d*-system. Note that $\Delta\cdot = \partial^2\cdot/\partial z^2 + \nabla^2\cdot$, $\langle f,g\rangle = \int_{-h(x)}^{0} f(z)g(z)\,\mathrm{d}z$, $\|f\|^2 = \langle f,f\rangle$, and δ_{nm} is Kronecker's delta

	$m=-1;\ n=-1,0,1,2,\ldots$	$m=0,1,2,\ldots;\ n=-1$	$m=0,1,2,\ldots;\ n=0,1,2,\ldots$
$a_{mn}(x,y)$	$\langle Z_{-1}, Z_n\rangle$	$\langle Z_m, Z_{-1}\rangle$	$\delta_{nm}\|Z_m\|^2$
$b_{mn}(x,y)$	$2\langle Z_{-1}, \nabla Z_n\rangle$	$2\langle Z_m, \nabla Z_{-1}\rangle$	$2\langle Z_m, \nabla Z_n\rangle + \nabla h Z_m(-h)Z_n(-h)$
$c_{mn}(x,y)$	$\langle Z_{-1}, \Delta Z_n\rangle$	$\langle Z_m, \Delta Z_{-1}\rangle + (1+\nabla h\nabla Z_{-1}(-h))Z_m(-h)$	$\langle Z_m, \Delta Z_n\rangle + \nabla h Z_n(-h)Z_m(-h)$

for the function ϕ_d in $\tilde{D}(R_\infty)$ to be

$$A(\tilde{D}(R_\infty)) = \{\chi(x,y,z)\in C^2(\tilde{D}(R_\infty)) \cap C^1(\tilde{D}(R_\infty)\cup\partial\tilde{D}(R_\infty))\}, \tag{4.2}$$

the variational formulation of the reduced diffraction problem takes the form:

$$\delta\mathscr{F}(\phi_\mathrm{d}) = 0, \qquad \phi_\mathrm{d}\in A(\tilde{D}(R_\infty)). \tag{4.3}$$

The equivalence between Eq. (4.3) and the diffraction problem can be easily shown by calculating the first variation $\delta\mathscr{F}$ of the functional [32,34], obtaining the following variational equation:

$$\begin{aligned}
&-\int_{\tilde{D}(R_\infty)}(\nabla^2\phi_\mathrm{d})\,\delta\phi_\mathrm{d}\,\mathrm{d}V + \int_{\partial\tilde{D}_\mathrm{F}(R_\infty)}\left(\frac{\partial\phi_\mathrm{d}}{\partial n} - \mu\phi_\mathrm{d}\right)\delta\phi_\mathrm{d}\,\mathrm{d}S\\
&+\int_{\partial\tilde{D}_\mathrm{II}(R_\infty)}\left(\frac{\partial\phi_\mathrm{d}}{\partial n} + g\right)\delta\phi_\mathrm{d}\,\mathrm{d}S\\
&+\int_{\partial\tilde{D}_V^{(1)}(R_\infty)}\left(\frac{\partial\phi_\mathrm{d}}{\partial n} - \mathrm{i}k_0^{(1)}\phi_\mathrm{d}\right)\delta\phi_\mathrm{d}\,\mathrm{d}S\\
&+\int_{\partial\tilde{D}_V^{(3)}(R_\infty)}\left(\frac{\partial\phi_\mathrm{d}}{\partial n} - \mathrm{i}k_0^{(3)}\phi_\mathrm{d}\right)\delta\phi_\mathrm{d}\,\mathrm{d}S\\
&+\int_{\partial\tilde{D}_V^{(2)}(R_\infty)}\left(\frac{\partial\phi_\mathrm{d}}{\partial n}\right)\delta\phi_\mathrm{d}\,\mathrm{d}S = 0.
\end{aligned} \tag{4.4}$$

In Eq. (4.4), $\partial\phi_\mathrm{d}/\partial n$ denotes the (outward) normal derivative of the diffraction potential on each part of the boundary. In particular, at the bottom boundary, the normal derivative takes the form

$$\frac{\partial\phi_\mathrm{d}}{\partial n} = -\left(\frac{\partial\phi_\mathrm{d}}{\partial z} + \nabla h\cdot\nabla\phi_\mathrm{d}\right)\frac{1}{\sqrt{1+(\nabla h)^2}}. \tag{4.5}$$

The proof of the equivalence of the variational Eq. (4.4) and the diffraction problem is completed by using standard arguments of the calculus of variations.

4.2. The d-system

Let us reconsider the variational principle (4.4) assuming that the diffraction field ϕ_d in $\tilde{D}(R_\infty)$ is represented by the enhanced local-mode series

$$\phi_\mathrm{d}(x,y,z) = \varphi_{-1}(x,y)Z_{-1}(z;x,y) + \varphi_0(x,y)Z_0(z;x,y) + \sum_{n=1}^{\infty}\varphi_n(x,y)Z_n(z;x,y). \tag{4.6}$$

In the above representation, the vertical functions $Z_m(z;x,y)$ are given, at every point (x,y) of the horizontal plane $\partial\tilde{D}_\mathrm{F}(R_\infty)$, by equations similar to Eqs. (3.2a), (3.2b) and (3.3c), with $h_i(x)$ being replaced by $h(x,y)$. The diffraction modal-amplitude functions $\varphi_n(x,y)$, $n=-1,0,1,\ldots$ will be distinguished from the corresponding ones for the incident field $\varphi_n(x)$, $n=-1,0,1,\ldots$ by the number of their arguments. The representation (4.6) identically satisfies the free-surface boundary condition, Eq. (2.10b), because of the choice of the vertical functions $Z_n(z;x,y)$. Similarly as in the case of the incident field, Eq. (3.3b), the sloping-bottom mode of the diffraction potential, defined by $\varphi_{-1}(x,y) = [\partial\phi_\mathrm{d}(x,y,z)/\partial z]_{z=-h}$, vanishes in constant-depth subregions. By substituting Eq. (4.6) in Eq. (4.4), we note that the term on the free-surface is identically zero, and using Eq. (4.5), the following coupled-mode system of equations for the diffraction problem is derived:

$$\begin{aligned}
&\sum_{n=-1}^{\infty} a_{mn}(x,y)\nabla^2\varphi_n(x,y) + \mathbf{b}_{mn}(x,y)\cdot\nabla\varphi_n(x,y)\\
&\quad + c_{mn}(x,y)\varphi_n(x,y) = g_m(x,y),\\
&m=-1,0,1,\ldots,\ (x,y)\in\partial\tilde{D}_\mathrm{F}(R_\infty),
\end{aligned} \tag{4.7}$$

supplemented by the following boundary conditions

$$\sum_{n=-1}^{\infty} a_{mn}(x,y)\left(\frac{\partial\varphi_n(x,y)}{\partial\nu} - \mathrm{i}k_0^{(1)}\varphi_n(x,y)\right) = 0, \tag{4.8a}$$
$$m=-1,0,1,\ldots,\ (x,y)\in\partial^2\tilde{D}_\mathrm{V}^{(1)}(R_\infty),$$

$$\sum_{n=-1}^{\infty} a_{mn}(x,y)\left(\frac{\partial\varphi_n(x,y)}{\partial\nu} - \mathrm{i}k_0^{(3)}\varphi_n(x,y)\right) = 0, \tag{4.8b}$$
$$m=-1,0,1,\ldots,\ (x,y)\in\partial^2\tilde{D}_\mathrm{V}^{(3)}(R_\infty),$$

$$\sum_{n=-1}^{\infty} a_{mn}(x,y)\frac{\partial\varphi_n(x,y)}{\partial\nu} = 0, \tag{4.8c}$$
$$m=-1,0,1,\ldots,\ (x,y)\in\partial^2\tilde{D}_\mathrm{V}^{(2)}(R_\infty),$$

where $\partial^2\tilde{D}_\mathrm{V}^{(l)}(R_\infty) = \partial(\partial\tilde{D}_\mathrm{V}^{(l)}(R_\infty))$, $l=1,2,3$, denote the projections of the parts of the vertical boundary $\partial^2\tilde{D}_\mathrm{V}^{(l)}(R_\infty)$ on the mean free surface ∂D_F, and $\vec{\nu}$ is the projection of the (outward) normal vector $\vec{n}$ on ∂D_F.

The forcing $g_m(x,y)$, $m=-1,0,1,2,\ldots$ of the *d*-system is

defined by

$$g_m(x,y) = -\left(\frac{\partial\phi_i(x,y,-h)}{\partial z} + \nabla h\cdot\nabla\phi_i(x,y,-h)\right) \times Z_m(-h;x,y) = g(x,y)Z_m(-h;x,y), \tag{4.9}$$

and the coefficients a_{mn}, $\mathbf{b}_{mn}$, c_{mn} are given in Table 1. These coefficients are distinguished from the corresponding ones involved in the *i*-system, Eq. (3.4), again by the number of their arguments. It is obvious that the support of the forcing $g_m(x,y)$, $m=-1,0,1,2,\ldots$, of the *d*-system is the same as the support of the localized scatterer(s). Moreover, since $Z_{-1}(-h;x,y)=0$, see Eq. (3.3c), the function $g_{-1}(x,y)=0$, everywhere.

If we restrict our attention to the class of monotonic background bed profiles $h_i(x)$, in order to avoid wave trapping in the strip $D^{(2)}$, it is expected from the far-field behaviour of the diffraction potential, Eqs. (2.12) and (2.12b), that the *d*-propagating mode $\varphi_0(x,y)$ will be at most of order $O(R^{-1/2})$, as $R\to\infty$. On the other hand, $\varphi_n(x,y)$ $n\neq 0$, will exhibit a faster decay as $R\to\infty$. This is true as $x\to\alpha_1$ or as $x\to\alpha_2$ in $D^{(2)}$, since the depth there eventually becomes constant, and thus, the sloping-bottom mode $\varphi_{-1}(x,y)=[\partial\phi_d(x,y,z)/\partial z]_{z=-h}$ vanishes, and all $\varphi_n(x,y)$ $n\geq 1$, behaves like the evanescent eigenmodes of the modified Helmholtz equation. Furthermore, for $\alpha_1<x<\alpha_2$ and $|y|$ large in $D^{(2)}$, all modes $\varphi_n(x,y)$, $n=-1,0,1,2,\ldots$, exhibit a faster decay of the order $O(R^{-3/2})$, as implied by the radiation condition (2.12b).

Thus, at large distances from the localized scatterer(s), the wavelike behaviour of the *d*-system is substantially determined by the propagating ($n=0$) mode. Therefore, moving away from the area $D_C^{(2)}$ (Fig. 1), all modes except the *d*-propagating mode can be approximately neglected. In this case, the system (4.7) reduces exactly to the homogeneous modified mild-slope equation [5,6,8]:

$$\nabla^2\varphi_0(x,y) + \frac{\nabla(cc_g)}{(cc_g)}\nabla\varphi_0(x,y) + k_0^2(1+\psi)\varphi_0(x,y) = 0, \quad (x,y)\in D/D_C^{(2)}. \tag{4.10}$$

In Eq. (4.10), $c=c(x,y)$ and $c_g=c_g(x,y)$ are the local phase and group velocities, respectively, and $k_0(x,y)$ is the local propagating wavenumber. The function $\psi=\psi(x,y)$ is dependent on the gradient and the curvature of the depth function.

A difficulty associated with the numerical solution of the *d*-system (4.7) is that the support $\partial\tilde{D}_F(R_\infty)$ of the modal amplitude functions $\varphi_n(x,y)$, $n=-1,0,1,2,\ldots$, has to be extended in a large part of the mean free surface ∂D_F, in order to avoid undesirable reflections from the boundary conditions (4.8a)–(4.8c). This difficulty can be greatly alleviated by introducing an absorbing layer as the closure condition of the *d*-system, located at the borderline of $D_C^{(2)}$ in the horizontal plane, as shown by using thick dashed lines in Fig. 1. In Section 5 the PML model, introduced by Berenger [26], will be adopted and optimized to serve as the closure condition of the *d*-system, in replacement of the boundary conditions (4.8a)–(4.8c).

5. The PML model as a closure condition of the diffraction problem

The basic feature of the perfectly matched layer (PML) model is that, by properly modifying the coefficients of the *d*-system in a finite-thickness layer surrounding the central region $D_C^{(2)}$, away from the three-dimensional bathymetric features, the diffraction wave energy that reaches this area is rapidly attenuated, avoiding the contamination of the numerical solution by spurious reflections. The derivation of a complete version of the *d*-system in the finite subdomain $[\alpha_1,\alpha_2]\times[\beta_1,\beta_2]$, with a PML-model closure, will be performed in two steps. First, the PML model will be implemented to the modified mild-slope Eq. (4.10), which is approximately describing the behaviour of the *d*-system in the area of the absorbing layer, and optimum PML coefficients will be derived in terms of the local value of the propagating wavenumber. Then, the consideration will be generalized to the *d*-system (4.7), taking into account that any spurious reflections might come out essentially from the interaction with the propagating mode. To begin with, we consider the modified mild-slope Eq. (4.10), which by means of the substitution $F=\sqrt{cc_g}\varphi_0$ reduces to the 2D Helmholtz equation

$$\nabla^2 F + k^2 F = 0, \tag{5.1}$$

where

$$k^2(x,y) = k_0^2(1+\psi) - \frac{\nabla^2\sqrt{cc_g}}{\sqrt{cc_g}}. \tag{5.2}$$

Locally, in the neighbourhood of any point P at the absorbing layer, Fig. 2, the wavenumber $k(x,y)$ can be considered constant. Introducing local coordinates $(\tilde{x},\tilde{y})$, with the $\tilde{x}$-axis taken to be normal to the absorbing layer, any outgoing solution of Eq. (5.1) in this neighbourhood can be analysed into plane waves of wavelength $\lambda=2\pi/k$, incident from various directions from $\tilde{x}<0$, and propagating into the absorbing layer $0<\tilde{x}<l$ (of thickness l). Inside the absorbing layer, the PML model for the Helmholtz equation, as provided by Turkel and Yefet [27] and Collino and Monk [28], reads

$$\frac{1}{s_x}\left(\frac{\partial}{\partial\tilde{x}}\left(\frac{1}{s_x}\frac{\partial F}{\partial\tilde{x}}\right)\right) + \frac{\partial^2 F}{\partial\tilde{y}^2} + k^2 F = 0, \tag{5.3}$$

where

$$s_x = s(\tilde{x}) = 1 + \frac{\mathrm{i}\sigma(\tilde{x})}{k}, \quad \sigma(\tilde{x})>0, \text{ for } \tilde{x}>0, \text{ and } \sigma(0)=\sigma'(0)=\sigma''(0)=0, \tag{5.4}$$

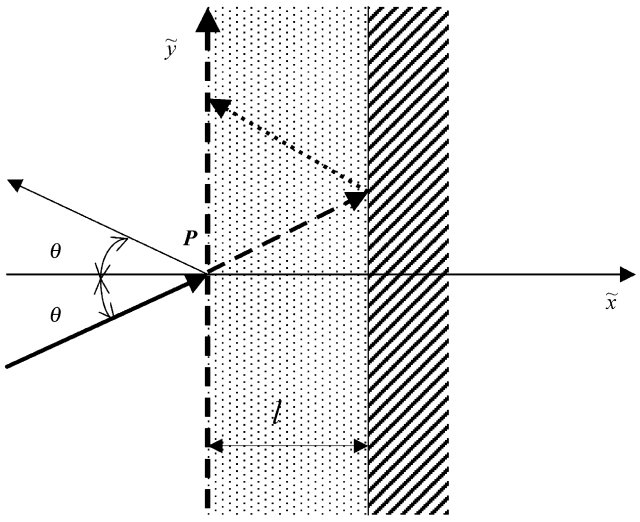

Fig. 2. Definition sketch of the PML model, locally at some place in the border of the truncated horizontal domain.

and a prime denotes differentiation with respect to $\tilde{x}$. In Eq. (5.3), $s_x = s(\tilde{x})$ is the PML coefficient which varies only across the absorbing layer. The models (5.3) and (5.4) are completed by a termination, e.g. Robin, boundary condition at the end of the layer $\tilde{x} = l$:

$$AF(\tilde{x} = l) + B\frac{\partial F(\tilde{x} = l)}{\partial \tilde{x}} = 0, \tag{5.5}$$

where A, B are constants. As follows from the PML literature [26,28], the specific choice of the coefficients A, B appears to be of minor importance. This is reasonable, since the model is aiming to attenuate the wave energy entering the layer, mainly during the 'propagation' phase, so that only a tiny fraction of it reaches the termination boundary at $\tilde{x} = l$. Moreover, the reflected (at $\tilde{x} = l$) energy continues to attenuate during the 'back propagation' phase, as approaches the interface $\tilde{x} = 0$ again.

5.1. Analysis of the PML reflection coefficient in the high frequency limit

Consider a plane wave incident at an arbitrary angle θ from $\tilde{x} < 0$ to the interface $\tilde{x} = 0$ of the absorbing layer $0 < \tilde{x} < l$. By expressing the wave potential in $\tilde{x} < 0$ as a superposition of incident and reflected components, and using WKB analysis, we obtain a high-frequency approximate solution to Eq. (5.3) in $0 < \tilde{x} < l$, for $\theta \neq \pi/2$, subjected to the termination condition (5.5). This solution, leads to the following result concerning the modulus of the PML reflection coefficient K_R

$$|K_R| \approx |\tau| \exp\left(-2\cos\theta \int_{t=0}^{t=1} \sigma(t)\,\mathrm{d}t\right), \tag{5.6}$$

where τ depends on the coefficients A, B of the termination condition. The basic feature of the PML model is the exponential decay of the reflection coefficient, which is governed by $\sigma(\tilde{x})$ and l. Berenger [26] introduced the following polynomial form for $\sigma(\tilde{x})$

$$\sigma(\tilde{x}) = \sigma_0(\tilde{x}/l)^n, \qquad n \geq 3, \tag{5.7a}$$

which when substituted in Eq. (5.6) leads to

$$|K_R| \propto \exp(-2\cos\theta\sigma_0 l/(n+1)). \tag{5.7b}$$

Thus, the efficiency of the PML model, in the high frequency limit, increases exponentially as $\sigma_0 l/(n+1)$ increases. In applications, the layer thickness l should remain relatively small, say of the order of 1 wavelength, since we are willing to keep the computational cost as low as possible. Having fixed the thickness, l, of the layer, the theoretical result (5.7b) indicates that a very high value of $\sigma_0 > 0$ and the smallest possible value of the exponent, $n = 3$, should produce the best results. However, in discretizing the PML equations by using a finite-difference scheme, additional factors enter into play, related with numerical reflections generated by the discretization. As shown by Collino and Monk [28], for a fixed number of points N per wavelength $\lambda = 2\pi/k$, the theoretical requirement of large $\sigma_0 > 0$ should be balanced with the requirement of smooth variation of the discretized $\sigma(\tilde{x})$, to ensure small numerical reflection.

5.2. The optimum discrete PML model

In implementing the discrete PML model, the following assumptions are introduced. (i) A fixed number N of grid-points per wavelength is used for discretizing the field equation by a finite-difference scheme (usually $N \geq 10$), and (ii) the grid spacing is kept the same both in the fluid domain and within the absorbing layer. Under these assumptions, optimum σ_0 and n values for the PML model (5.7a) are obtained by means of the merit function

$$R_m(n, \sigma_0 k^{-1}; l/\lambda, N) = \int_{\theta=0}^{\theta=\pi/2} \left|R_{dB}(\theta; n, \sigma_0 k^{-1}; l/\lambda, N)\right| \times (\cos\theta)^{1/4}\,\mathrm{d}\theta, \tag{5.8}$$

where $R_{dB} = -20\log_{10}|K_R|$ is the PML reflection coefficient, expressed for convenience in dB. The weight function $(\cos\theta)^{1/4}$ is used in order to put more emphasis in the range of directions from normal incidence, $\theta = 0$, up to $\theta \approx \pi/3$, which are most important for our purposes. For the calculation of the reflection coefficient appearing in Eq. (5.8) under the integral, the PML equations are discretized and numerically solved by using a second-order finite difference scheme. Then, the corresponding optimization problems are solved with respect to n and $\sigma_0 k^{-1}$, for the parameters l/λ and N taking values in the ranges $l/\lambda \in [0.5, 2]$ and $N \in [7, 20]$. It is worth mentioning that the final results remain practically the same by using either a Neumann or a Dirichlet termination condition for the PML model.

As an example, the distributions of the optimum discrete PML reflection coefficient $R_{dB,opt}(\theta; l/\lambda, N)$, obtained by the

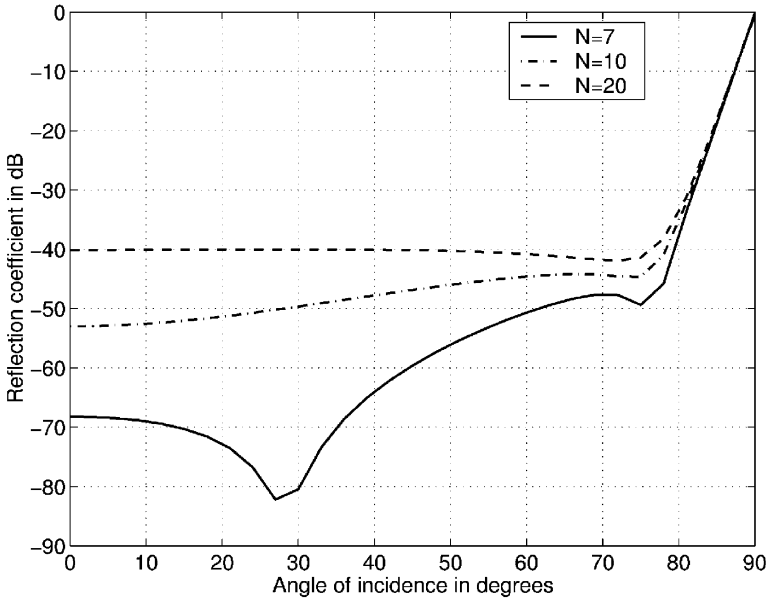

Fig. 3. Optimum PML reflection coefficients for layer thickness $l/\lambda = 1$ and various discretizations corresponding to $N = 7$ (solid line), $N = 10$ (dash-dot line) and $N = 20$ (dashed line) points per wavelength.

optimization of Eq. (5.8), are presented in Fig. 3 vs. the angle of incidence θ, for a layer thickness $l/\lambda = 1$ and three typical resolutions (numbers of gridpoints per wavelenth) $N = 7$, 10, 20. From this figure we can see that, by using the PML model (5.7a) with grid resolution $N = 10$ (dash-dot line), the reflection coefficient remains below 1% (or −40 dB) for angles of incidence up to almost $\theta = 80°$. As the layer thickness and the grid resolution increase, the efficiency of the PML model becomes even better.

5.3. The PML d-system

On the basis of the above analysis, we proceed now to couple the PML model with the *d*-system. The area D_{PML} of the absorbing layer of uniform thickness l, surrounding the horizontal computational domain (as shown by thick dashed line in Fig. 1), is the part of the mean free surface enclosed by the rectangles $D_{\alpha\beta} = \{\alpha_1 \le x \le \alpha_2, \beta_1 \le y \le \beta_2\}$ and $\hat{D}_{\alpha\beta} = \{\hat{\alpha}_1 \le x \le \hat{\alpha}_2, \hat{\beta}_1 \le y \le \hat{\beta}_2\}$, where $\hat{\alpha}_1 = \alpha_1 - l$, $\hat{\beta}_1 = \beta_1 - l$, $\hat{\alpha}_2 = \alpha_2 + l$, $\hat{\beta}_2 = \beta_2 + l$. Recalling that in this area the forcing of the *d*-system is zero, and assuming that the coefficient matrix a_{mn} is non-singular, we obtain from Eq. (4.7)

$$\sum_{n=-1}^{\infty} \delta_{mn}\nabla^2\varphi_n(x,y) + (a_{mn})^{-1}(\mathbf{b}_{mn}(x,y)\cdot\nabla\varphi_n(x,y) + c_{mn}\varphi_n(x,y)) = 0, \quad m = -1, 0, 1, \ldots. \tag{5.9}$$

Since the wavelike behaviour of the system for $(x,y) \in D_{\mathrm{PML}}$ is essentially determined by the propagating ($n = 0$) mode, a straightforward approach is to substitute, at the next step, the horizontal Laplacian operator appearing in Eq. (5.9) by the PML operator D^2, defined as follows:

$$D^2\varphi_n = \begin{cases} \dfrac{1}{s_x}\left(\dfrac{\partial}{\partial x}\left(\dfrac{1}{s_x}\dfrac{\partial\varphi_n}{\partial x}\right)\right) + \dfrac{1}{s_y}\left(\dfrac{\partial}{\partial y}\left(\dfrac{1}{s_y}\dfrac{\partial\varphi_n}{\partial y}\right)\right), & n = 0 \\ \nabla^2\varphi_n, \quad n \neq 0 \end{cases} \tag{5.10}$$

In Eq. (5.10), s_x is given by Eq. (5.4) and s_y is defined similarily. These coefficients are calculated in terms of the local value of the propagating wavenumber $k_0(x,y)$ in the absorbing layer D_{PML} by means of the optimization of Eq. (5.8). Extending these functions by unity for all points outside the absorbing layer, $(x,y) \in D_{\alpha\beta}$, and transforming back the system to its normal form by left multiplication with the matrix a_{mn}, we obtain finally PML *d*-system:

$$\sum_{n=-1}^{\infty} a_{mn}(x,y)D^2\varphi_n(x,y) + \mathbf{b}_{mn}(x,y)\cdot\nabla\varphi_n(x,y) + c_{mn}(x,y)\varphi_n(x,y) = g_m(x,y), \quad m = -1, 0, 1, \ldots, \quad (x,y) \in \hat{D}_{\alpha\beta}. \tag{5.11}$$

6. Numerical results and discussion

The discrete scheme for the numerical solution of the *i*-system, Eqs. (3.3a)–(3.3c) and (3.4), has been presented in Athanassoulis and Belibassakis [1], and will not be discussed herein. In this section, the discrete scheme for the numerical solution of the PML *d*-system, Eq. (5.11), is presented and discussed. Then, numerical results are presented for the scattering by an elliptic shoal superimposed over a sloping bottom, and compared with

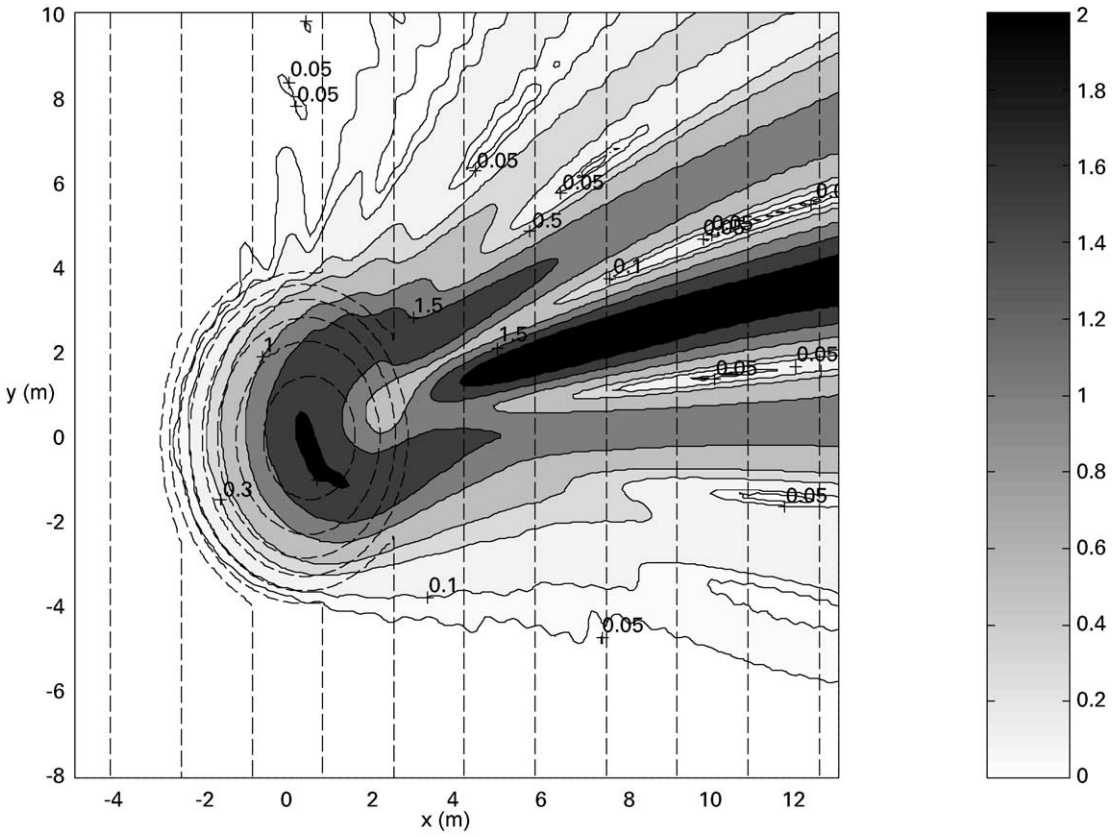

Fig. 4. Bathymetry of the elliptic shoal over a 2% sloping bottom [9], and contours of the modulus of the diffraction wave field $|\phi_d|$ on the free surface, as calculated by the present method.

experimental measurements and numerical results obtained by means of the modified mild-slope (Eq. (4.10)). In this case, the bottom slope is small and thus, the mild-slope is adequate to describe the wave field. In order to better illustrate the effect of steeper bottom slopes on the calculated wave field, a second geometry corresponding to a steep platform reef with bottom corrugations is examined, and the results obtained using the present method and the modified mild-slope equation are compared and discussed.

6.1. Discrete approximation of the coupled-mode system of equations

Truncating the series (4.6) to a finite number of terms (modes), and denoting by N_e the number of evanescent modes retained in the representation, the following approximation of the diffraction wave potential is obtained

$$\phi_d(x,y,z) = \sum_{n=-1}^{N_e} \varphi_n(x,y) Z_n(z;x,y). \tag{6.1}$$

The total number of modes retained is $N_m = N_e + 2$. The construction of the discrete system is completed by using central, second-order finite differences to approximate the derivatives of the amplitude functions $\varphi_n(x,y)$ in the PML d-system (5.11). The system is supplemented by using Neumann-type termination conditions of the PML model at $x = \hat{\alpha}_1$ and $x = \hat{\alpha}_2$, and at $y = \hat{\beta}_1$ and $y = \hat{\beta}_2$, respectively. The coefficient matrix of the obtained algebraic system is block structured, each block being composed by a sparse band-diagonal submatrix of dimension N_d. The forcing $g_n(x,y)$ of the discrete system is non-zero only for the gridpoints falling inside the support of $h_d(x,y)$, and $g_{-1}(x,y) = 0$ throughout the whole domain $\hat{D}_{\alpha\beta}$. As concerns the numerical solution of the linear algebraic system, a direct method, based on Gaussian elimination, is used for $N_d \leq 300\,000$, requiring a computation time of order of 10 CPU minutes in a Pentium III 500 MHz machine. For larger systems, an iterative solution has been implemented, based on the hierarchy of the magnitude of the modes.

Let us make here some additional comments concerning our choice to formulate and solve the problem with respect to the diffraction potential ϕ_d instead of the total wave potential ϕ; see Eq. (2.6). In numerically solving a scattering problem using finite differences, two kinds of error are introduced by the discretization procedure (i) the amplitude error, which is of order $O(k^p s^p)$ for a pth-order finite difference scheme with grid spacing s, and (ii) the phase error, which grows linearly with the distance from the forcing of the system, at a rate of order $O(k^{p+1}s^p)$ [35]. In

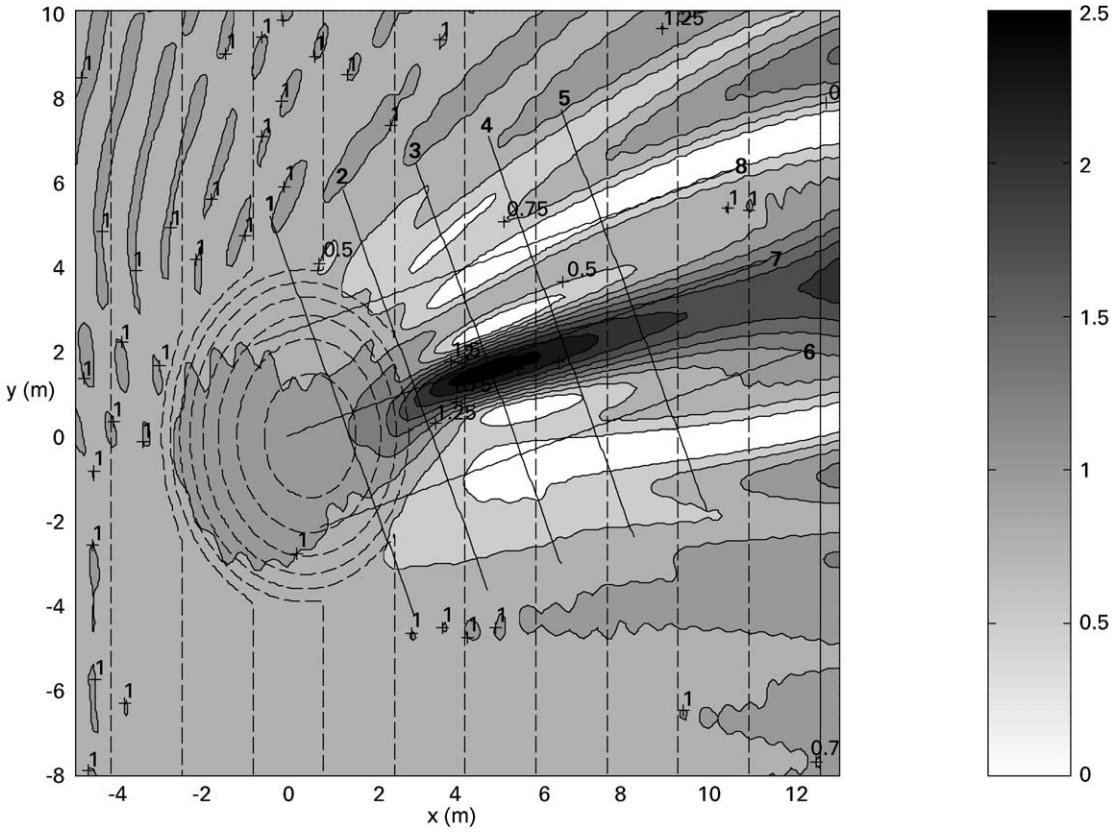

Fig. 5. Bathymetry as in Fig. 4 and contours of the modulus of the total wave field $|\phi|$ on the free surface, as calculated by the present method. The experimental measurements, reported by Berkhoff et al. [9], refer to sections 1–8 shown by using solid lines.

the formulation with respect to the total wave potential, the forcing of the system applies through a boundary condition to the offshore boundary, which is usually located far from the area of the localized scatterer(s). On the contrary, in the formulation with respect to the diffraction wave potential, the forcing has the same support as the localized scatterer(s). Thus, working with the diffraction potential we obtain numerical solutions of superior quality in the area around the scatterer(s), since the growing phase error travels significantly less distance.

6.2. Presentation of numerical results and discussion

6.2.1. The case of an elliptic scatterer over a sloping bottom

As a first example, we consider here the scattering by an elliptic shoal superimposed over a sloping bottom of constant slope 2%, studied by Berkhoff et al. [9]. In this case, the background bathymetry $h_i(x)$ (the constant slope supporting the elliptic shoal) is defined as follows

$$h_i(x) = \begin{cases} 0.45, & x < -5.85 \\ 0.45 - 0.02(5.85 + x), & -5.85 \le x \le 14.15 \\ 0.05, & x > 14.15 \end{cases} \tag{6.2a}$$

and the disturbance $h_d(x, y)$ produced by the localized scatterer is given by

$$h_d(x, y) = \begin{cases} 0, & (x/3)^2 + (y/4)^2 > 1 \\ 0.3 - 0.5\sqrt{1 - (x/3.75)^2 - (y/5)^2}, & (x/3)^2 + (y/4)^2 \le 1 \end{cases}, \tag{6.2b}$$

where all distances are in metres. For this environment, experimental data are available from Ref. [9], for an incident wave of period $T = 1$ s, propagating at an angle $\theta_1 = 20^\circ$ with respect to the small semi-axis of the elliptical scatterer. In this case, the shallowness ratio is varying from $h_1/\lambda_1 = 0.3$, in the deep-water region, to $h_3/\lambda_3 = 0.075$, at the shallow end of the sloping bottom. Thus, everywhere in the variable bathymetry region, and especially in the neighbourhood of the scatterer, the shallowness ratio falls well outside the limits of application of the deep or the shallow water theory. All numerical results presented in Figs. 4–6 refer to the above environment and wave conditions.

The maximum bottom slope of the above environment appears at the front side of the scatterer, facing the incident wave, and is 18%. Let it be noted that, in this example, the bed slope is rather small, and thus, the mild-slope equation can be considered to be adequate for calculating the wave field. Nevertheless, this example has been selected as a case study in the present work, because experimental data are

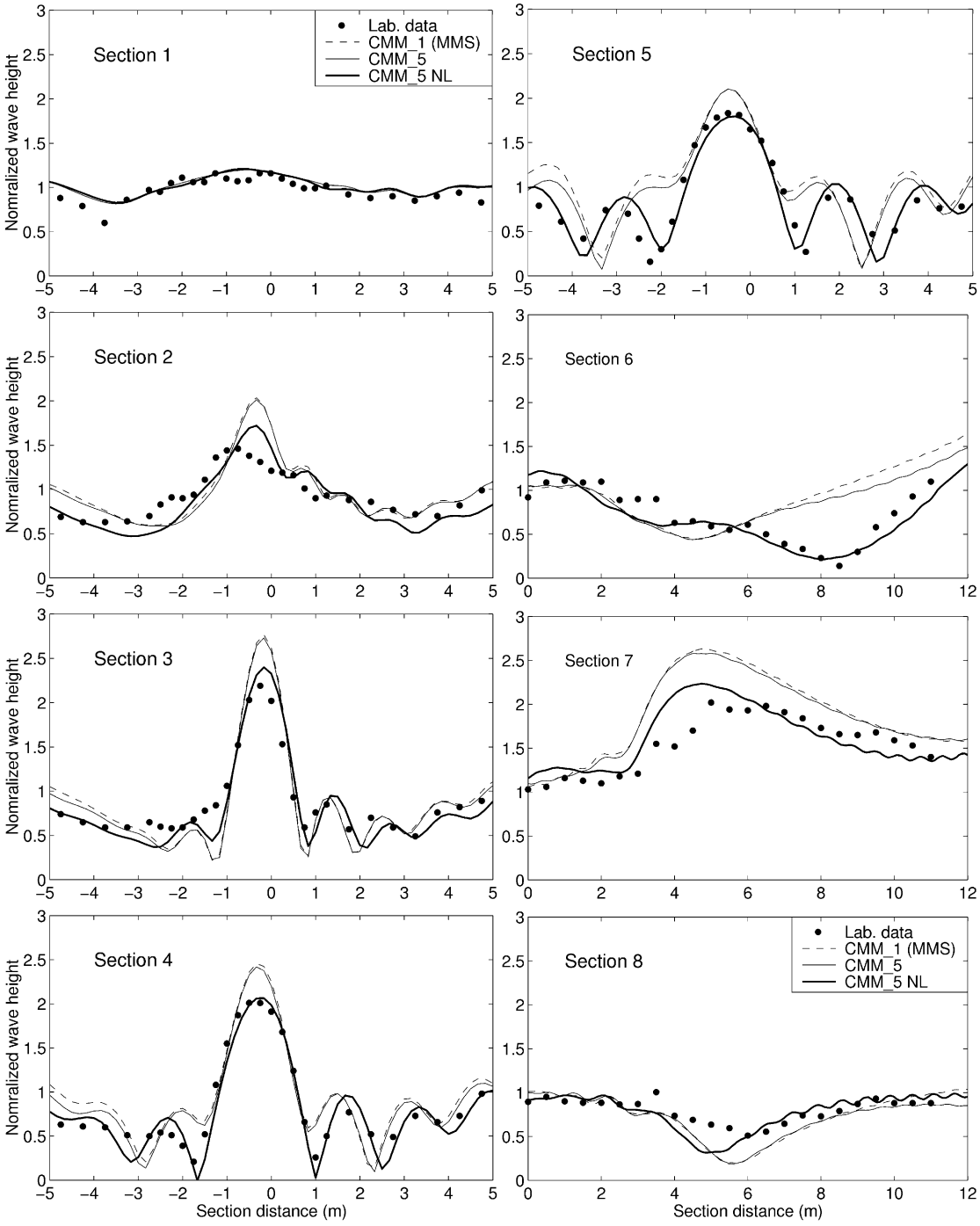

Fig. 6. Normalized wave height along sections 1–8 of Fig. 5. Comparison between the experimental data from Berkhoff et al. [9], the numerical results obtained by the modified mild-slope equation (CMM_1 (MMS), shown by dashed lines), the present method using five modes (CMM_5, shown by thin solid lines), and the present method with non-linear corrections (CMM_5 NL, shown by thick solid lines).

available to compare with, and because it has been used by many researchers as a benchmark problem. The bathymetric contours along with the calculated modulus of the diffraction and the total wave potential on the free-surface, in the area around the localized scatterer, are illustrated in Figs. 4 and 5, respectively, as obtained by the present method. Numerical results shown have been obtained by subdividing the ranges $\hat{\alpha}_2 - \hat{\alpha}_1 = 25$ m and $\hat{\beta}_2 - \hat{\beta}_1 = 20$ m into $N_x = N_y = 231$ segments, which corresponds to 10 points per wavelength on the average. In Fig. 4 we observe that the contours representing equal-amplitude lines of the modulus of the diffraction potential on the free-surface are smooth, i.e. the calculated pattern does not appear to be contaminated by spurious reflections. This implies that the

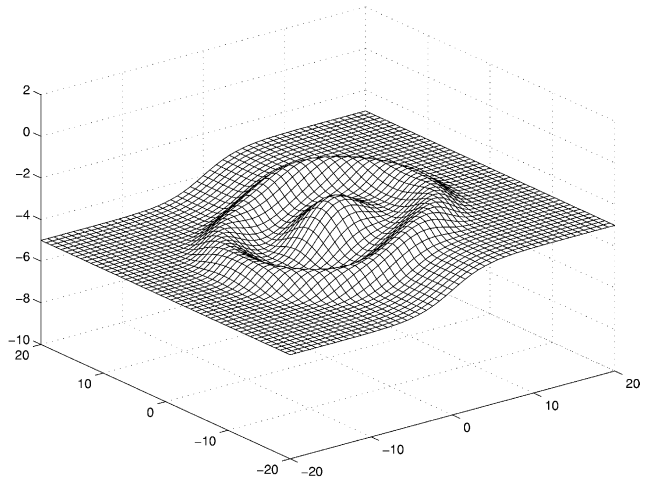

Fig. 7. Three-dimensional plot of a steep platform reef with bottom corrugations. The bathymetry is defined by Eqs. (6.6a) and (6.6b).

PML-model closure of the *d*-system operates efficiently, absorbing almost all outgoing wave energy.

It must be mentioned here that the present method does not require any alignment of the computational domain with the direction of the oblique-incident wave. This is due to the fact that we solve independently the incident and the diffraction problems. In this way, the problem on the incident field is reduced to a two-dimensional problem, Eqs. (2.8a)–(2.8f), which is solved by implementing the complete matching-boundary conditions, while the diffraction field is solved by means of the PML *d*-system, which is able to absorb the diffraction energy coming from any direction. Thus, the whole numerical solution is insensitive to the direction of incidence θ_1, as far as the latter is not very close to $\pi/2$.

Comparisons between the results obtained by the present coupled-mode system predictions using five modes (CMM_5) and laboratory data, concerning the normalized wave height, are presented in Fig. 6. Also, in the same figure, the corresponding results by the modified mild-slope (MMS) are plotted by using dashed lines. The latter have been obtained by the present code, by retaining only the propagating mode ($n = 0$) in the representations of both the incident and the diffraction fields, and solving Eqs. (3.3a)–(3.3c) and (4.7) only for the propagating mode. The experimental measurements, reported by Berkhoff et al. [9], refer to sections 1–8 shown in Fig. 5 by using solid lines and annotated by corresponding numbers. As already discussed, in this example the bed slope is small, and thus, MMS results (annotated as CMM_1) are quite close to the coupled-mode method ones. Specific discrepancies between the present method results and experimental data, as, e.g. the overestimation of the focal peak in sections 2, 3 and 7, the misalignment of the wave field along section 5, and the lack of prediction of the trough along section 6, are due to the non-linear effects (see Dalrymple et al. [12], Fig. 7), that are not modelled by the present (linear) theory. This discrepancy can be remedied by introducing non-linear corrections, using the second-order, amplitude-dependent dispersion relation proposed by Kirby and Dalrymple [36], and also used by Panchang et al. [13]. An iterative approach for including weakly non-linear effects has been implemented to the present method, and the results are also plotted in Fig. 6, using a thick line (annotated as CMM_5 NL). We can observe from this figure that the agreement between present method results and experimental data is substantially improved.

As concerns the rate of convergence of the representations (3.1) and (4.6) of the incident and the diffraction fields, respectively, extensive numerical experience of the present authors (demonstrated also in Figs. 5 and 6 and discussed in detail in Section 6.2 of Ref. [1]), has shown that, the corresponding modal amplitude functions $\varphi_n(x)$ and $\varphi_n(x,y)$ exhibit a decay of the order $O(n^{-4})$, uniformly with respect to x and y

$$|\varphi_n(x)|, |\varphi_n(x,y)| = O(n^{-4}), \qquad n \to \infty. \tag{6.3}$$

Eq. (6.3) suggests that only a few modes are sufficient in order to accurately calculate the fully three-dimensional wave field up to (and including) the boundaries. For example, in the present test case, $N_m = 5$ ($N_e = 3$) modes are enough to limit the error due to the truncation of the infinite series of the diffraction field to less than 0.001. Another interesting conclusion drawn from the present results, and supported by extensive numerical experience, is that the amplitude of the slopping-bottom mode is comparable in magnitude to the amplitude of the propagating mode in subregions of appreciable bottom slope. Even if the bottom slope is small, the sloping-bottom mode, being also small, is an order of magnitude (or more) greater than the first evanescent mode (see Fig. 5 of Ref. [1]). We summarise the above hierarchy of the mode amplitudes as follows:

mild-slope case :

$$O(|\varphi_0|) \geq O(|\varphi_{-1}|) \geq O(|\varphi_1|) \geq \cdots O(|\varphi_n|) \geq O(|\varphi_{n+1}|) \cdots \tag{6.4}$$

steep-slope case :

$$O(|\varphi_0|) \approx O(|\varphi_{-1}|) \geq O(|\varphi_1|) \geq \cdots O(|\varphi_n|) \geq O(|\varphi_{n+1}|) \cdots \tag{6.5}$$

This result justifies the concept and the usefulness of the sloping-bottom mode φ_{-1}.

6.2.2. The case of steep platform reef with bottom corrugations

As a second example, we consider the case of an idealized platform reef with bottom corrugations. A three-dimensional plot of the bottom surface of this environment is shown in Fig. 7. In this case, the background bathymetry $h_i(x)$ (the 2D

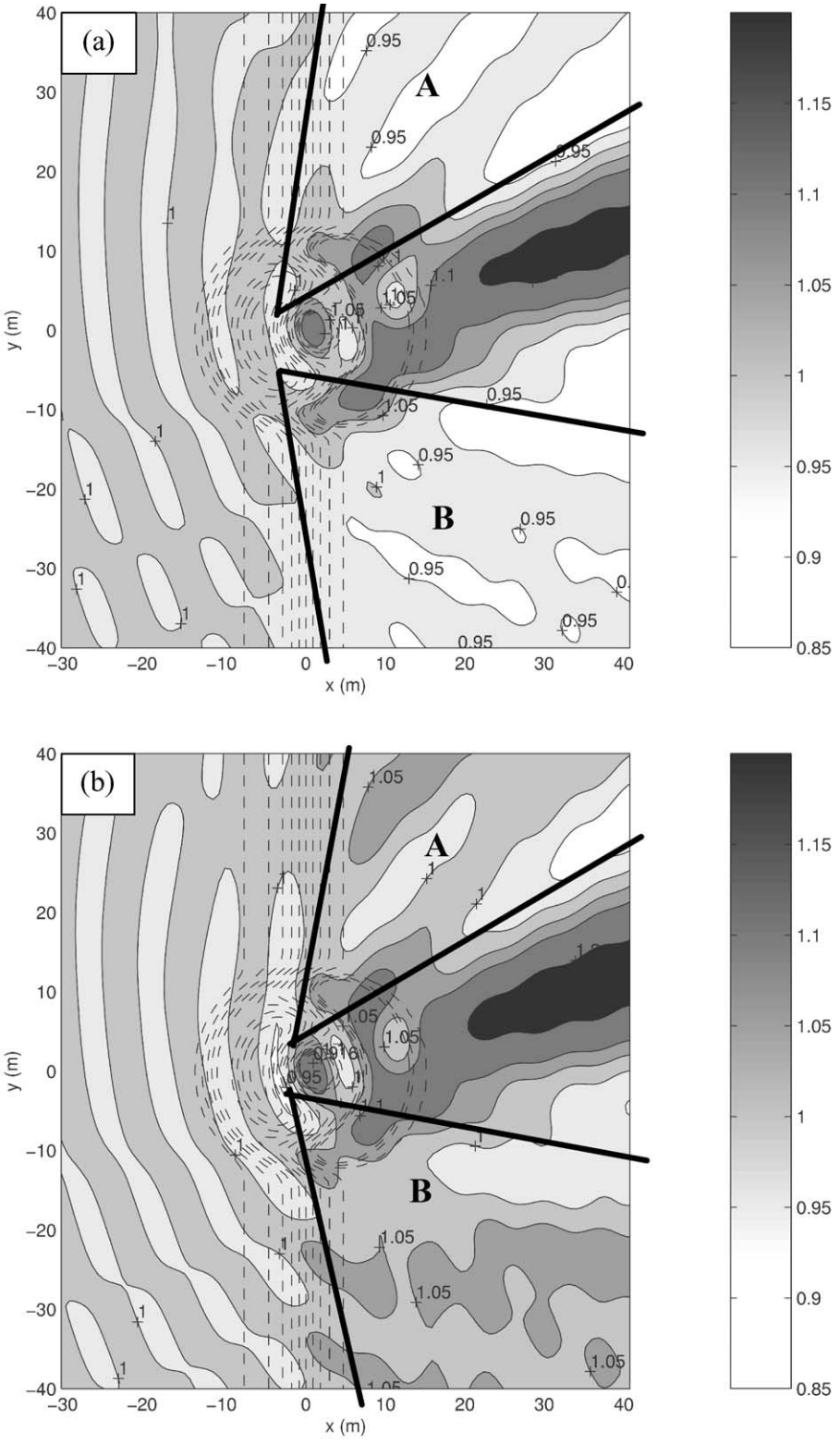

Fig. 8. Comparison between (a) the modified mild-slope equation results, and (b) the present method results, concerning the wave pattern on the free surface, for the steep platform reef with bottom corrugations (shown in Fig. 7). Contours of the modulus of the total wave field $|\phi(x, y, z = 0)|$. Wave frequency $\omega = 2$ rad/s. Wave height $H = 1$ m. The bathymetric contours are also shown by using dashed lines.

sloaling supporting the 3D bathymetric features) is selected to be given by

$$h_i(x) = \begin{cases} h_1 = 5, & x < -20 \\ \dfrac{h_1 + h_3}{2} - \dfrac{h_1 - h_3}{2}\tanh\left(3\pi\left(\dfrac{x+20}{40} - \dfrac{1}{2}\right)\right), & -20 < x < 20, \\ h_3 = 3, & x > 20 \end{cases} \tag{6.6a}$$

where all distances are in metres. The depth disturbance $h_d(x, y)$ is defined by

$$h_d(x, y) = 0.5\, h_A(1 + \cos(KR))\exp(-(R/L)^8), \qquad R = \sqrt{x^2 + y^2}, \tag{6.6b}$$

leading to bottom corrugations of length $L = 2\pi/K = 12$ m and amplitude $0.5h_A = 0.75$ m, that gradually vanish outside the cylinder of radius $R = 12$ m. The maximum bottom slope in this environment is 50%, i.e. almost three times higher than the previous case. The wave field is taken to be excited by an incident wave of period $T = 3.41$ s ($\omega = 2$ rad/s), propagating at an angle $\theta_1 = 20°$ with respect to x-axis (the centerline of the scatterer). In this case, the shallowness ratio is varying from $h_1/\lambda_1 = 0.33$ in the deep-water region to $h_3/\lambda_3 = 0.22$ at the shallow end of the sloping bottom (Eq. (6.6a)).

Extensive comparisons between the present method (obtained by using five modes in the representations) and the modified mild-slope results, concerning the horizontal bottom velocities and the wave potential (or pressure) at the bottom, have shown that the modified mild-slope underestimates the amplitudes of the horizontal bottom velocity and of the bottom pressure. The differences are concentrated in the area of the three-dimensional scatterer and are maximized as its middle and rear tops, where the depth is minimum. These differences are considered significant, especially as concerns the exploitation of the results for further studies, as e.g. the calculation of oscillating bottom boundary layer and wave-energy dissipation due to bottom friction, as well as for sea-bed movement and sediment transport.

To illustrate further the differences between the present method and the modified mild-slope equation results, a comparison is presented in Fig. 8, concerning the calculated wave patterns on the free surface. In this figure the bathymetric contours along with the calculated modulus of the total wave potential on the free surface (which is the same as the free-surface elevation normalized with respect to the amplitude of the oblique-incident wave) are plotted, in the area around the localized scatterer of Fig. 7. Focusing Fig. 8, we observe that, at the rear part of the scatterer, in the sectors designated as 'A' and 'B' outside the focal region, the differences between the modified mild-slope (top) and the present method (bottom) are of the order of 5–10%. In these areas the present method exhibits an increased total wave energy, which should be attributed to stronger diffraction due to fine-scale three-dimensional wave-bottom interactions that cannot be well resolved by the modified mild slope model. Let it be noted that, the free surface is the part of the field where the results obtained by the present coupled-mode system and the modified mild-slope equation exhibit the least discrepancy.

7. Concluding remarks

A consistent coupled-mode theory has been derived for calculating the diffraction of small-amplitude water waves by localized scatterers superimposed over a parallel-contour bathymetry. The present method does not introduce any simplifying assumptions or other restrictions concerning either the bottom slope and curvature, or the vertical structure of the wave field. All wave phenomena (refraction, reflection, diffraction) are fully modelled and, thus, the present method can serve as a useful tool for the analysis of the wave field in the whole range of parameters within the regime of linear theory.

A key feature of the present method is the introduction of an additional mode, completely describing the influence of the bottom slope. It turns out that the presence of the additional mode in the series representation of the potential makes it consistent with the bottom boundary condition and substantially accelerates its convergence. The obtained coupled-mode system of horizontal equations presents a number of advantages as (i) only a few modes (e.g. 3–5) are sufficient to accurately calculate the wave field in the whole liquid domain; (ii) the enhanced coupled-mode system can be naturally simplified either to the extended mild-slope equation or to the modified one in subareas where the physical conditions permit it; (iii) owing to a successful coupling between the diffraction system and the PML absorbing layer model, the support of the d-system can be restricted to an area a little larger than the support of the three-dimensional bathymetric features, offering a great reduction in computational cost; (iv) The present method provides high-quality information concerning the pressure and the tangential velocity at the bottom, which is useful for the study of oscillating bottom boundary transport studies. Finally, the analytical structure of the present model facilitates its extension to various directions as, e.g. to wave-current systems or to the weakly non-linear (second and higher order) wave interactions in a variable bathymetry region.

References

[1] Athanassoulis GA, Belibassakis KA. A consistent coupled-mode theory for the propagation of small-amplitude water waves over variable bathymetry regions. J Fluid Mech 1999;389:275–301.

[2] Berkhoff JCW. Computation of combined refraction–diffraction, Proceedings of the 13th ICCE. Vancouver: ASCE, 1972. p. 471–90.

[3] Mei CC. The applied dynamics of ocean surface waves. 2nd reprint. Singapore: World Scientific, 1994.

[4] Kirby JT. A general wave equation for waves over rippled beds. J Fluid Mech 1986;162:171–86.
[5] Massel S. Extended refraction–diffraction equations for surface waves. Coast Engng 1993;19:97–126.
[6] Chamberlain PG, Porter D. The modified mild-slope equation. J Fluid Mech 1995;291:393–407.
[7] Booij N. A note on the accuracy of the mild-slope equation. Coast Engng 1983;7:191–203.
[8] Miles JW, Chamberlain PG. Topographical scattering of gravity waves. J Fluid Mech 1998;361:175–88.
[9] Berkhoff JCW, Booij N, Radder AC. Verification of numerical wave propagation models for simple harmonic linear water waves. Coast Engng 1982;6:255–79.
[10] Tsay TK, Liu PLF. A finite element model for wave refraction and diffraction. Appl Ocean Res 1983;5(1):30–7.
[11] Dalrymple RA, Kirby JT. Models for very wide-angle water waves and water diffraction. J Fluid Mech 1988;192:33–50.
[12] Dalrymple RA, Suh KD, Kirby JT, Chae JW. Models for very wide-angle water waves and wave diffraction. Part 2. Irregular bathymetry. J Fluid Mech 1989;201:299–322.
[13] Panchang VG, Pearse BR, Wei G, Cushman-Roisin B. Solution of the mild-slope wave problem by iteration. Appl Ocean Res 1991;13(4): 187–99.
[14] Li B. A generalized conjugate gradient method for the mild-slope equation. Coast Engng 1994;23:215–26.
[15] Zhao Y, Anastasiou K. Modelling of wave propagation in the near-shore region using the mild-slope equation with GMRES-based iterative solvers. Int J Numer Meth Fluids 1996;23:397–411.
[16] Oliveira FSBF, Anastasiou K. An efficient computational model for water wave propagation in coastal regions. Appl Ocean Res 1998;20: 263–71.
[17] Li B, Anastasiou K. Efficient elliptic solvers for the mild-slope equation using the multigrid technique. Coast Engng 1992;16:245–66.
[18] Porter D, Staziker DJ. Extension of the mild-slope equation. J Fluid Mech 1995;300:367–82.
[19] Porter D, Chamberlain PG. Linear wave scattering by two-dimensional topography. In: Hunt JN, editor. Gravity waves in water of finite depth. Southampton: Computational Mechanics Publications, 1997. p. 13–53.
[20] Chandrasekera CN, Cheung KF. Linear refraction–diffraction model for steep bathymetry. J Wtrwy Port Coast Ocean Engng 2001; 127(3):161–70.
[21] Athanassoulis GA, Belibassakis KA. Water wave Green's function for a 3D uneven bottom problem with different depths at $x \rightarrow +\infty$ and $x \rightarrow -\infty$. In: Geers ThL, editor. IUTAM Symposium on Computational Methods for Unbounded Domains, Fluid mechanics and its applications, vol. 39. 1998. p. 21–32.
[22] Belibassakis KA. The Green's function of the mild-slope equation. The case of the monotonic bed profile. Wave Motion 2000;32:339–61.
[23] Givoli D. Non-reflecting boundary conditions. J Comput Phys 1991;94:1–29.
[24] Dalrymple RA, Martin PA. Perfect boundary conditions for parabolic water-wave models. Proc R Soc Lond A 1992;437:41–54.
[25] Tsynkov SV. Numerical solution of problems in unbounded domain. Appl Numer Meth 1998;27:465–532.
[26] Berenger J-P. A perfectly matched layer for the absorption of electromagnetic waves. J Comput Phys 1994;114:185–200.
[27] Turkel E, Yefet A, Absorbing PML. boundary layers for wave-like equations. Appl Numer Meth 1998;27:533–57.
[28] Collino F, Monk PB. Optimizing the perfectly matched layer. Comput Meth Appl Mech Engng 1998;164:157–71.
[29] Kirby JT, Dalrymple RA. Propagation of obliquely incident waves over a trench. J Fluid Mech 1983;133:47–63.
[30] Longuet-Higgins MS. On the trapping of wave energy round islands. J Fluid Mech 1967;29:781–821.
[31] Bai KJ. A variational method in potential flows with a free surface, Rep. NA 72-2. Berkeley: College of Engineering, University of California, 1972.
[32] Bai KJ, Yeung RW. Numerical solution to free-surface flow problems, Proceedings of the 10th Naval Hydrodynamics Symposium. Cambridge, MA: Office of Naval Research, 1974. p. 609–41.
[33] Yeung RW. Numerical methods in free-surface flows. Ann Rev Fluid Mech 1982;14:395–442.
[34] Mei CC, Chen HS. A hybrid element method for steady linearized free surface flows. Int J Numer Meth Engng 1976;10:1153–75.
[35] Bayliss M, Goldstein CI, Turkel E. On accuracy conditions for the numerical computation of waves. J Comput Phys 1985;59:396–404.
[36] Kirby JT, Dalrymple RA. An approximate model for nonlinear dispersion in monochromatic wave propagation models. Coast Engng 1986;9:545–61.